Single-Loop Droop Control Strategy for a Grid-Connected DFIG Wind Turbine

I. Oraa, *Graduate Student Member, IEEE*, J. Samanes, *Member, IEEE*, J. Lopez, *Member, IEEE*, and E. Gubia, *Member, IEEE*

***Abstract*—When grid-forming droop control strategies are implemented in grid-connected power converters, two control strategies are widely used; the single-loop and multi-loop droop controls. However, only multi-loop droop control strategies with inner control loops have been implemented in doubly-fed induction generator (DFIG)-based wind turbines so far. This paper proposes the application of a single-loop droop control strategy to a DFIG wind turbine, which has not been previously explored or implemented. As shown in the paper, the application of the conventional droop control without inner control loops to DFIG-based wind power systems does not ensure a stable response. After modeling the system dynamics and evaluating its stability, two causes of instability have been identified; a resonance at the rotor electrical frequency relevant at high slips, and a phase margin reduction at low slips. To solve these instability issues two control solutions are proposed; the emulation of a virtual resistor, and a phase rotation. The proposed control strategy allows stabilizing the system and achieving a fast and damped dynamic response. The effectiveness of the proposed control strategy is validated by experimental results.**

***Index Terms*—Doubly-fed Induction Generator (DFIG), Control design, Droop Control, Grid-forming, Stability Analysis.**

I. Introduction

Synchronous generators (SGs) of conventional fossil-fuel power plants have been responsible for controlling the power grid since its inception. However, in the coming years, these generators will be gradually replaced by renewable energies (RREE) such as wind power, which, along with photovoltaic, is set to lead the transition towards a generation system based on renewable energy sources [1].

Doubly-fed induction generator (DFIG)-based wind turbines are the most prevalent technology in onshore wind farms [2]. As RREE, such as DFIG-based wind farms, replace SGs, grid strength and stability may be put at risk. This is due to the fact that most grid-connected power converters are controlled as current sources, in what is known grid-following (GFL) mode, under the assumption that the grid is a stiff voltage source. As a result, they do not contribute to system strength and stability. System strength denotes the resilience of the voltage waveform to withstand disturbances, so when system strength is reduced, stability issues are more likely to arise [3]. If a power converter operates in GFL mode, the voltage that the converter imposes is distorted during grid transients in order to regulate the current waveform. Therefore, GFL power converters reduce system strength. In recent years, the development of grid-forming (GFM) control strategies has attracted particular interest [4]–[6]. In contrast to GFL power converters, GFM power converters behave as voltage sources that regulate the grid voltage and frequency. These converters can enhance the power system strength by imposing a voltage waveform resilient to grid transients.

Among GFM control strategies, droop control is widely known [7], [8]. In droop-controlled grid-connected power converters generally two control loops are included; an active power-frequency loop (P-ω) and a reactive power-voltage loop (Q-V), which adjust the phase angle and amplitude of the converter output voltage, respectively. When GFM droop control strategies are implemented in grid-connected power converters, whether in photovoltaic, battery storage or full-converter wind power systems, two similar droop controls are widely used; the single-loop, i.e., without inner loops, and multi-loop, i.e., with inner loops, controls. In [9] a comprehensive comparative study is conducted to understand the fundamental differences between these two basic controls. Although being very similar, the results of the study show that the single-loop droop control has a larger small-signal stability limit, while the multi-loop droop control is prone to be less damped and loses stability more easily under some circumstances.

The single-loop droop control, has shown certain advantages in terms of small signal stability when is applied to grid-connected power converters. However, when droop control strategies are applied to DFIG wind turbines, multi-loop control strategies with inner control loops have always been implemented so far. In [10]–[13] the indirect stator flux orientation (ISFO) based droop control is implemented. Two outer control loops, a P-ω droop control and a Q-V droop control, determine the stator frequency and voltage amplitude, respectively. Then, the stator voltage is controlled by the stator voltage control loop that regulates the excitation current and provides the d-axis rotor current reference for an inner current control loop. The q-axis reference is adjusted so that the stator flux at the q-axis is zero. Thus, the stator flux is

Paper [1], presented at the 2022 IEEE 23rd Workshop on Control and Modeling for Power Electronics (COMPEL), Tel Aviv, Israel, 20-23 June, 2022. This work was supported by the Spanish State Research Agency (AEI) under grant PID2019-110956RB-I00 /AEI/ 10.13039.

I. Oraa, J. Samanes, J. Lopez and E. Gubia are with the Electrical, Electronic and Communications Engineering, and Institute of Smart Cities, Public University of Navarre, Campus de Arrosadia, 31006 Pamplona, Spain. (Corresponding author: Iker Oraa, E-mail: iker.oraa@unavarra.es)

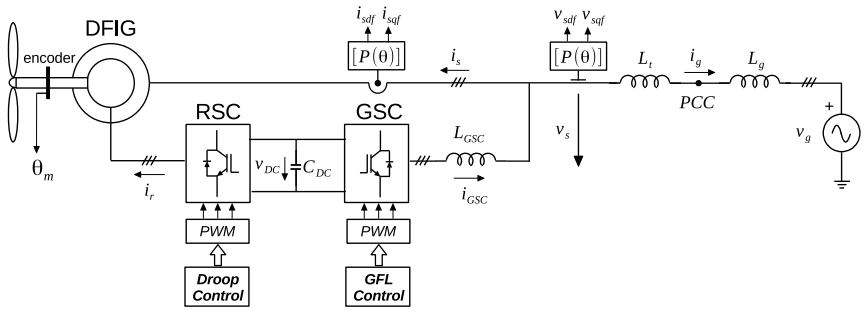

Fig. 1. Grid-connected DFIG wind turbine.

oriented along the d-axis. In [14] two outer droop control loops that generate the reference stator frequency and voltage amplitude are also implemented, but in this case a cascade voltage and current control is implemented. The stator voltage control loops determine the references for the inner rotor current control loops that adjust the rotor voltage to track these references.

Unlike the conventional approach where inner control loops are typically used, this paper proposes the application of a single-loop droop control strategy to a DFIG wind turbine, which has not been previously explored or implemented. However, as it is demonstrated in [1], the application of the conventional droop control without inner control loops to DFIG-based wind power systems does not ensure a stable response. System dynamics is especially influenced by the machine's rotational speed, and in most operating points the system response is unstable. Therefore, the conventional droop control strategy should be adapted to the specific characteristics of DFIG wind turbines in order to achieve a stable response.

This paper further develops the work presented in [1], where a single-loop droop control strategy is proposed to provide DFIG-based wind turbines with GFM characteristics. On the one hand, this paper proposes the implementation of a transient phase rotation to stabilize the system. This transient phase rotation stabilizes the system and decouples the control loops in steady state, which overcomes the limitations of the control proposed in [1] due to the coupling introduced in steady state. On the other hand, in this paper the influence of grid strength on system stability is analyzed, and the robustness of the proposed control strategy to grid strength variations is verified. Additionally, the performance of the proposed single-loop droop control strategy under load variations and unbalances is compared with a multi-loop control method applied to DFIG wind turbines. Finally, the proposed control strategy is validated through experimental results, and the capability of the proposed control to provide frequency support under grid frequency variations is demonstrated.

The paper is organized as follows. Section II describes the system under study and the single-loop droop control to be implemented. In Section III system stability is evaluated and the causes of instability are identified. In Section IV, the control solutions to stabilize the system response are proposed, and an optimization process to adjust the optimal control parameters is carried out. In Section V the proposed control solutions are validated in an experimental setup. Finally, the conclusions are drawn in Section VI.

II. System Description

The system under study, illustrated in Fig. 1, represents a grid-connected DFIG wind turbine. The rotor-side converter (RSC) is connected directly to the rotor and is responsible for controlling the stator active and reactive power. The grid-side converter (GSC) is connected to the stator terminals via the inductor, L_{GSC}. The GSC regulates its output current, i_{GSC}, in order to provide a stable voltage, v_{DC}, in the DC-link capacitor, C_{DC}. The wind turbine is connected to the grid at the point of common coupling (PCC) through a step-up transformer, which is modeled by a leakage inductance L_t. The grid is modeled as an ideal voltage source and a series inductor L_g. The voltages v_s and v_g represent the stator and grid voltages, and the currents i_s, i_r, and i_g the stator, rotor, and grid currents, respectively.

The system is controlled in the synchronous reference frame or dq-axis by aligning the rotor voltage along the d-axis. In the GSC a GFL control is applied, while in the RSC a single-loop droop control, i.e., without inner control loops, is implemented. The droop control strategy is depicted in Fig. 2. On the one hand, the Q-V control loop regulates the module of the RSC output voltage. A PI controller, with a proportional gain K_p and integral time constant T_n, provides an increase in

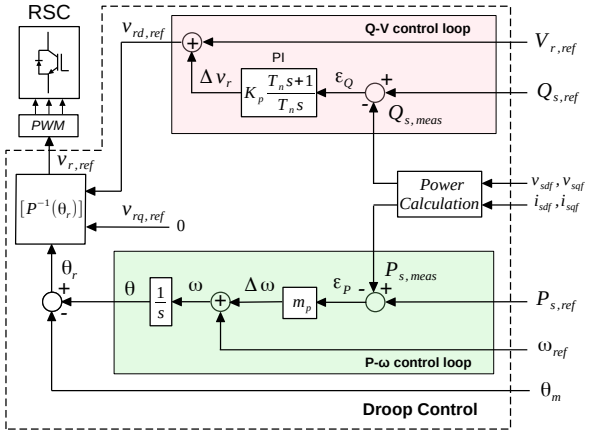

Fig. 2. Single-loop droop control scheme for the RSC.

the rotor voltage magnitude, Δv_r, to correct the reactive power error, ϵ_Q, computed as the difference between the reference reactive power, $Q_{s,ref}$, and the measured reactive power, $Q_{s,meas}$. This increase is added to the rotor reference voltage, $V_{r,ref}$, obtaining the rotor voltage in the d-axis, $v_{rd,ref}$. The q component of the rotor voltage, $v_{rq,ref}$, is zero so that the rotor voltage is oriented along the d-axis of the dq rotating frame.

On the other hand, the P-ω control loop regulates the frequency and phase of the rotor voltage to synchronize the converter with the grid. The P-ω control loop provides a frequency increase, $\Delta\omega$, proportional to the active power error, ϵ_P, computed as the difference between the reference active power, $P_{s,ref}$, and the measured active power, $P_{s,meas}$, and to the P-ω droop coefficient, m_p. Similarly to synchronous machines' droop, the m_p coefficient represents the rate between the per unit frequency deviation, $\Delta f/f_n$, and the per unit power increment, $\Delta P/P_n$. This frequency increase is added to the reference frequency ω_{ref}, which is equal to the grid nominal frequency, to obtain the dq-axis rotational speed, ω. Then, by integrating ω, the angle θ is obtained. This angle defines the position of the dq rotating axis over a stationary reference frame with respect to the stator and it is used for the Park transformation of the stator variables. The angle θ_r required for the Park transformation of the rotor variables depends on the position of the rotor, θ_m, that is measured by the DFIG shaft encoder. By applying the inverse Park transformation, $[P^{-1}(\theta_r)]$, the instantaneous rotor voltages, $v_{r,ref}$, that the RSC will modulate, are obtained. The stator active and reactive powers are calculated by means of the filtered measurements of the stator voltages and currents in dq-axis, v_{sdf}, v_{sqf}, i_{sdf} and i_{sqf}.

It should be noted that the active power reference would be determined by a MPPT algorithm. Under normal operating conditions, when the grid frequency is at its nominal value, the output power tracks the MPPT power setpoint. However, when the grid frequency deviates from the nominal value, the output power automatically varies to correct that frequency variation. An operation based on the MPPT would not provide additional power during frequency drops. Therefore, if frequency support is desired during frequency drops, it is necessary to have some form of energy storage or operate below the maximum power point to have a power reserve available.

As indicated in [15], [16], the GSC has minimal impact on small-signal stability. Therefore, when evaluating system stability its influence is neglected.

III. Stability Analysis

In order to implement the single-loop droop control strategy represented in Fig. 2, an initial stability analysis is conducted using the small-signal model proposed in [17]. The block diagram representation of this model is depicted in Fig. 3. This model is based on the Park's vector approach and models the DFIG and its interaction with the RSC droop control, obtaining a Multiple-Input Multiple-Output (MIMO) dynamic model that accurately reproduces system stability and dynamics. The model is linearized around an operating point determined by the machine's rotational speed and the active and reactive power level. As shown in Fig. 3, the Q-V control loop regulates the rotor voltage amplitude, Δv_{rd}, to correct the reactive power error, ϵ_Q, while the P-ω control loop adjusts the frequency, $\Delta\omega$, and phase angle, $\Delta\theta$, according to the active power error, ϵ_P. The $DFIG + Grid$ block represents the plant of the system and models the dynamics of the stator voltages and currents, Δv_{sdq} and Δi_{sdq}, which are filtered by an analog low-pass filter, $[LPAF(s)]$, and used by the $[PQ]$ block to model the dynamics of stator active and reactive powers. The block $D_{conv}(s)$, included in the control diagram, models the delays introduced by the power converter, the computation delay of the DSP and the effect of the zero-order hold, which represents the PWM converter.

After implementing the model in $MATLAB$, the stability of the system has been analyzed considering the system parameters defined in Table I. The P-ω droop coefficient, m_p, is defined by grid codes, so the P-ω control loop is already adjusted. In order to adjust the parameters of the PI controller, K_p and T_n, the system stability is analyzed by means of the Multiple-Input Multiple-Output Generalized

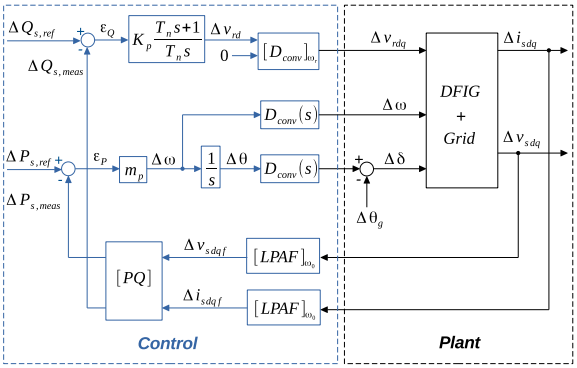

Fig. 3. Block diagram representation of the small-signal model used to analyze system stability.

TABLE I
System Parameters

Parameter	Magnitude
Grid $S_B = 2$ *MVA*, $U_g = 20$ *kV*, $F_g = 50$ H_z	
Line reactance	0.0995 p.u.
Line resistance	0.01 p.u.
Wind turbine transformer $S_B = 2$ *MVA*, $20/0.69$ *kV*	
Reactance	0.085 p.u.
DFIG (referred to stator) $S_{DFIG} = 2$ *MVA*, $U_{DFIG} = 690$ *V*	
Rotor resistance	0.0018 Ω
Rotor leakage inductance	76.3 μH
Stator resistance	0.0032 Ω
Stator leakage inductance	161 μH
Mutual inductance	0.0025 H
Pole pairs	2
Power converter control parameters	
Sampling frequency	5.7 kHz
P-ω droop coefficient	0.05 p.u.
PI proportional gain	4e-5 V/VAr
PI integral time constant	0.01 s
Cut-off frequency of low-pass analog filters	1500 Hz

Bode Criterion (MIMO-GBC), derived from the generalized Nyquist stability criterion [18]. This theory allows to analyze the stability of any MIMO system, such as the 2x2 dynamic model obtained for a DFIG wind turbine controlled in the synchronous reference frame, through the Bode diagram of the open-loop transfer function matrix eigenvalues. According to the MIMO-GBC, the number of closed-loop unstable poles, Z, is equal to the number of open-loop unstable poles, P, minus the total number of $\pm m180$ degrees crossings (m odd integer) with positive magnitude counted in the Bode diagram of all the system open-loop eigenvalues, C^+ (crossings with increasing phase), C^- (with decreasing phase) and C_0 (at 0 Hz)

$$Z = P - [2(C^+ - C^-) + C_0]. \quad (1)$$

The design objective is to obtain a cut-off frequency of 10 Hz and a minimum phase margin of 30 degrees in the eigenvalue linked to the Q-V control loop. As an example, the PI is adjusted at synchronism, i.e., at 1500 rpm. For this purpose, a time constant, T_n, equal to 0.01 s, and a proportional gain, K_p, equal to 4e-5 V/VAr are set. In Fig. 4 the Bode diagram of the open-loop transfer function matrix eigenvalues, that correlate output active and reactive powers, $P_{s,meas}$ and $Q_{s,meas}$, with power errors, ϵ_P and ϵ_Q, is represented for the synchronous speed. As shown in Fig. 4, with the tuned PI controller, the eigenvalue λ_1 (blue), linked to the P-ω loop, has a cut-off frequency of 1.34 Hz and a phase margin of 33.5 degrees, while the eigenvalue λ_2 (orange), linked to the Q-V loop, has a cut-off frequency of 10.7 Hz and a phase margin of 35.6 degrees. As can be observed, there is no -180 degree crossing with positive magnitude in the phase diagram of the eigenvalues, so, according to (1), as the system has no open-loop unstable poles (P = 0), the closed-loop system has no unstable poles, Z = 0. Therefore, the system is stable at 1500 rpm.

After tuning the PI controller and proving that the system is stable at 1500 rpm by means of the MIMO GBC theory, the stability of the system over the entire operating speed range of the machine is analyzed. For this purpose, the closed-loop poles of the system at different slips are obtained.

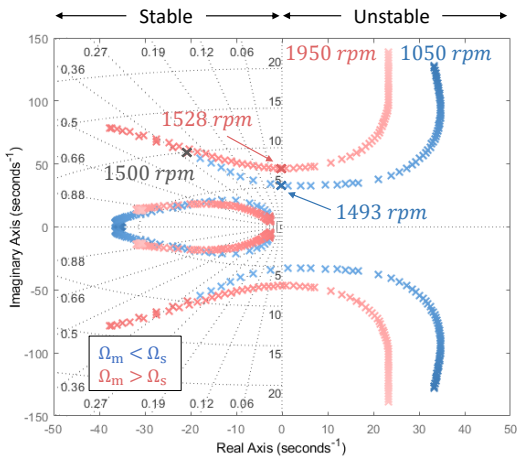

Fig. 5. Evolution of the closed-loop poles with the machine's rotational speed.

The slip is defined as $slip = (\Omega_s - \Omega_m)/\Omega_s$, where Ω_s is the synchronous speed and Ω_m is the machine's rotational speed. The slip varies between -30% and +30%. The grid nominal frequency, f_0, is 50 Hz and the machine has two pole pairs. Therefore, the operating speed varies from 1050 to 1950 rpm. Fig. 5 shows the evolution of the closed-loop poles with the machine's rotational speed. Below synchronism, i.e., at positive slips, the poles are plotted in blue, while above synchronism, i.e., at negative slips, they are represented in red. As shown in Fig. 5, the system is unstable across all operating speeds, except in a narrow range of rotational speeds between 1493 and 1528.

In order to identify the causes of instability, the eigenvalues of the open-loop transfer function matrix are analyzed in the frequency domain for a rotational speed far from synchronism, i.e., at high slips, and for a rotational speed close to synchronism, i.e., at low slips. On the one hand, as shown in Fig. 6 (solid lines), at 1050 rpm, there is a resonance at 15 Hz. This frequency corresponds to the rotor electrical frequency, f_r. As mentioned above, the grid nominal frequency, f_0, is 50 Hz, and

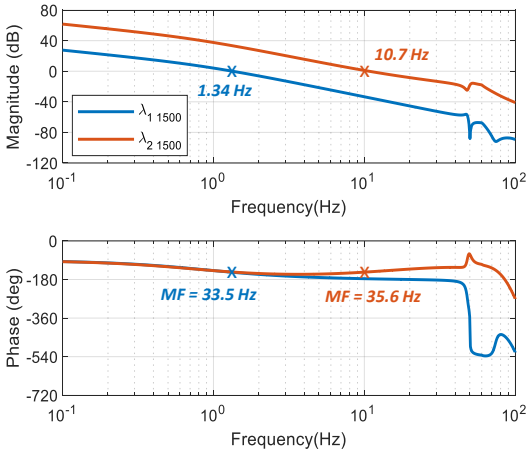

Fig. 4. Bode diagram of the open-loop transfer function matrix eigenvalues at Ω_m=1500 rpm.

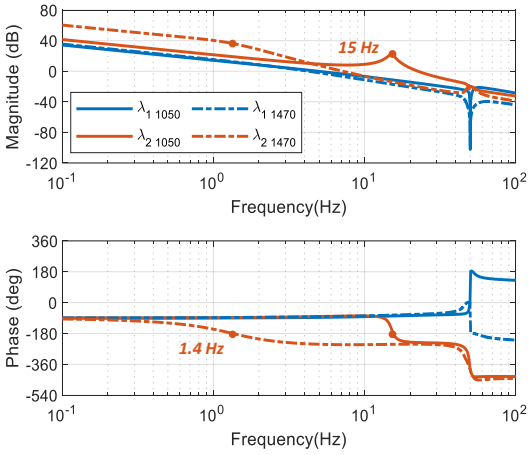

Fig. 6. Bode diagram of the open-loop transfer function matrix eigenvalues at Ω_m=1050 rpm (solid lines), and at Ω_m=1470 rpm (dashed lines).

at 1050 rpm the $slip = +0.3$, so the rotor electrical frequency, $f_r = slip f_0$, is 15 Hz. Therefore, the frequency at which this resonance occurs will vary with the machine's rotational speed. Due to this resonance, there is a -180 degree crossing with positive magnitude and decreasing phase (C^- = 1), marked by the orange dot, in the phase diagram of the eigenvalue λ_2, that introduces two closed-loop unstable poles, Z = 2. On the other hand, as observed in Fig. 6 (dashed lines), at 1470 rpm, this resonance is almost damped. However, the -180 degree crossing with positive magnitude and decreasing phase (C^- = 1), marked by the orange dot, still occurs around the rotor electrical frequency, 1 Hz in this case, due to the phase margin reduction of the eigenvalue λ_2. As a result, the closed-loop system still has two unstable poles, Z = 2.

In conclusion, there are two causes that contribute to system instability. Firstly, the resonance at the rotor electrical frequency, relevant at rotational speeds far from synchronism, i.e., at high slips. Secondly, the phase margin reduction at rotational speeds close to synchronism, i.e., at low slips. It is therefore evident that the conventional droop control without inner control loops must be adapted in order to be applicable to DFIG wind turbines. The control strategy proposed for this purpose is presented in the following section.

IV. Proposed Droop Control Strategy

As demonstrated in the preceding section, there are two causes of instability; a resonance at high slips, and a phase margin reduction at low slips. In order to apply a single-loop droop control in a DFIG wind turbine, two control solutions, depicted in red in Fig. 7, are proposed. The first solution involves the emulation of a virtual resistor that damps the resonance at the rotor electrical frequency, solving the first cause of instability. To solve the second cause of instability, a rotation that increases the phase margin in the most restrictive eigenvalue is applied.

A. Virtual Resistor Emulation

As shown in Fig. 6 (solid lines), at high slips, there is a resonance at the rotor electrical frequency that destabilize the system. To damp this resonance, a possible solution is to increase the machine's resistance value. This can be achieved by adapting the control to emulate a virtual resistor, as suggested in [19].

The basic idea involves modifying the RSC voltage in relation to the current. As shown in red in Fig. 7, the RSC voltage references, $v_{rd,ref}$ and $v_{rq,ref}$, are adjusted based on the stator current measurements, i_{sdf} and i_{sqf}, proportionally to the virtual resistor, $[R_v]$. Including this virtual resistor may result in an error in the steady-state reference voltage. To avoid this, a high-pass filter, $HPF_{R_v(s)}$, is incorporated. As the resonance moves with the rotor electrical frequency, the high-pass cut-off frequency is variable and equal to $\omega_{c,HPF_{R_v}}(s) = |2\pi f_r|/10$ rad/s.

As can be seen in Fig. 8, the emulation of a virtual resistor $R_v = 0.1\ p.u.$ at 1050 rpm damps the resonance at 15 Hz. This way, the -180 degree crossing with positive magnitude is avoided and the system is stabilized.

B. Transient Phase Rotation

As shown in Fig. 6, at low slips, this resonance is almost damped, and, as can be seen in the Bode diagram of Fig. 9 (solid lines), the emulation of a virtual resistor does not allow stabilizing the system. There are three -180 degree crossings with positive magnitude, one with increasing phase ($C^+ = 1$) and two with decreasing phase ($C^- = 2$), that introduce two unstable closed-loop poles.

Nevertheless, these crossings only occur in the eigenvalue λ_2, whereas the eigenvalue λ_1 has a sufficiently high phase margin. Therefore, by introducing a rotation in the open-loop transfer function matrix, the phase of the eigenvalue λ_2 can be increased and this -180 degree crossings can be avoided [20].

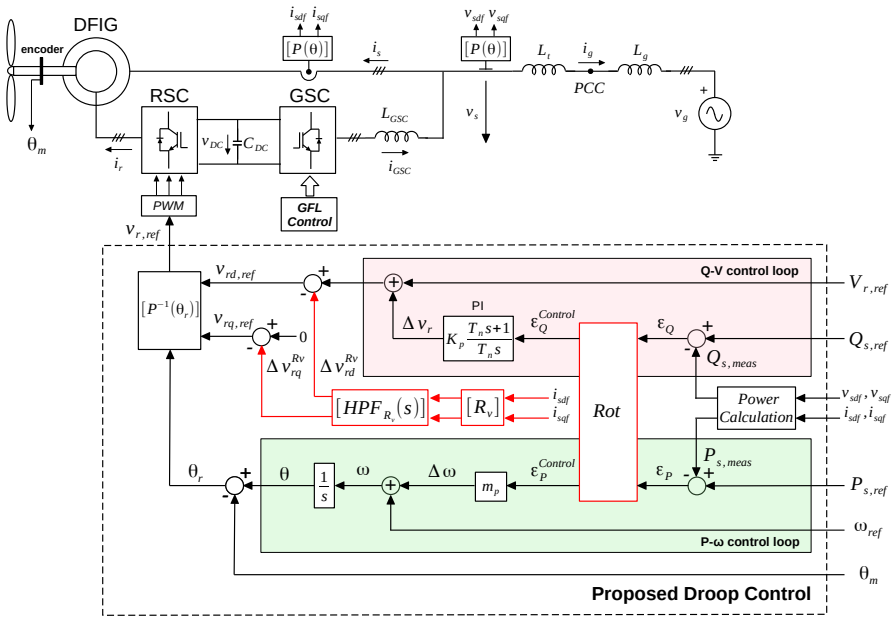

Fig. 7. Proposed single-loop droop control strategy for a DFIG wind turbine.

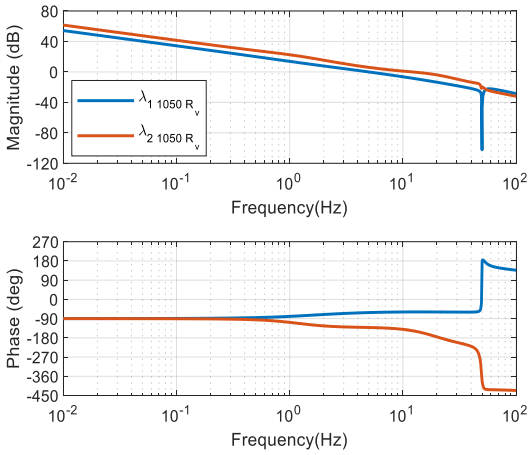

Fig. 8. Bode diagram of the open-loop transfer function matrix eigenvalues at Ω_m=1050 rpm with $R_v = 0.1\ p.u.$

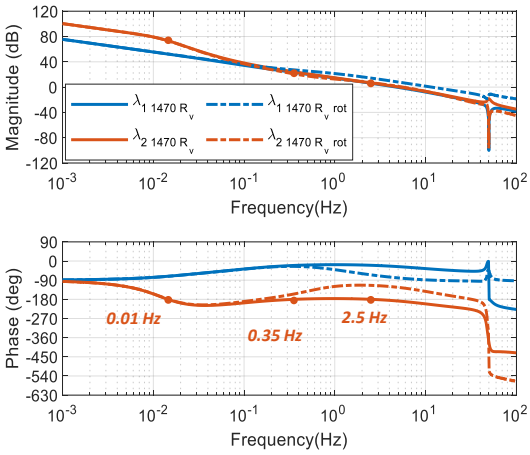

Fig. 9. Bode diagram of the open-loop transfer function matrix eigenvalues at Ω_m=1470 rpm, with $R_v = 0.1\ p.u.$ (solid lines), and $\alpha_R = 60°$ (dashed lines).

To achieve this, the application of a transient phase rotation is proposed. The implementation of this transient phase rotation is depicted in Fig. 10. The power errors are filtered by a high-pass filter, $HPF_{\epsilon_{PQ}}(s)$, and then they are rotated by α_R. This way, the rotation acts only on transients to stabilize the system response, and, in steady state, the power errors are decoupled, thus allowing to provide frequency support and ensuring reactive power tracking. The cut-off frequency of the high-pass filter is set to $\omega_{c,HPF_{\epsilon_{PQ}}} = 2\pi$ rad/s since the instability at low slips is produced at low frequency, in this case, as shown in Fig. 9, at 2.5 Hz.

As can be observed in Fig. 9 (dashed lines), applying a 60 degree rotation at 1470 rpm, the phase of the eigenvalue λ_2 increases avoiding the -180 degree crossing at 2.5 Hz and, thus, the system is stabilized.

C. Optimal control parameters

The system response can be stabilized at all rotational speeds by the combination of the virtual resistor and phase rotation. In order to achieve an improved response, for each operating point, these control parameters are adjusted through an optimization process. The objective of this optimization process is to minimize the root mean square error (RMSE) in the active and reactive power step response. In other words, the active and reactive power response is optimized in terms of overshoot and settling time. The objective function is defined in (2).

$$f_{obj} = min(RMSE_P + RMSE_Q), \tag{2}$$

where

$$RMSE_P = \sqrt{\sum_{k=1}^{N}(P_{s,meas}(k) - P_{s,ref}(k))^2/N}, \tag{3}$$

$$RMSE_Q = \sqrt{\sum_{k=1}^{N}(Q_{s,meas}(k) - Q_{s,ref}(k))^2/N}, \tag{4}$$

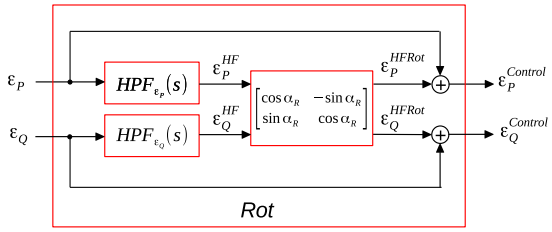

Fig. 10. Proposed transient phase rotation block diagram.

where $(P_{s,meas}(k) - P_{s,ref}(k))$ and $(Q_{s,meas}(k) - Q_{s,ref}(k))$ are the deviations of the active and reactive power time response with respect to the active and reactive power references at sample k, and N is the sample size.

This way, for each rotational speed and for each active and reactive power level, the optimal virtual resistor and phase rotation values, that minimize (2), are obtained. Therefore, the virtual resistor and phase rotation values are adaptive, i.e., for each operating point they have a different value. In Fig. 11 the optimal virtual resistor and phase rotation values for rotational speeds of 1050 and 1470 rpm are represented as a function of the active and reactive power. As can be seen in Fig. 11 (a), the resistance required at 1050 rpm is higher at all power levels compared to the resistance needed at 1470 rpm. Likewise, at both 1050 rpm and 1470 rpm, the required resistance value is higher as the active and reactive power levels increase. Regarding rotation, as can be observed in Fig. 11 (b), at 1050 rpm the required phase rotation increases as the active power level increases. In contrast, at 1470 rpm the rotation is more influenced by the reactive power level. Thus, at low reactive power levels a higher rotation is required at 1470 rpm, but as the reactive power level increases the required rotation is similar at both rotational speeds, and even higher at 1050 rpm.

Once the control parameters are adjusted, in Fig. 12 the evolution of the closed-loop poles with the machine's rotational speed is plotted again. As can be proved, there are no closed-loop poles with positive real part, so the system is stable over the whole operating speed range.

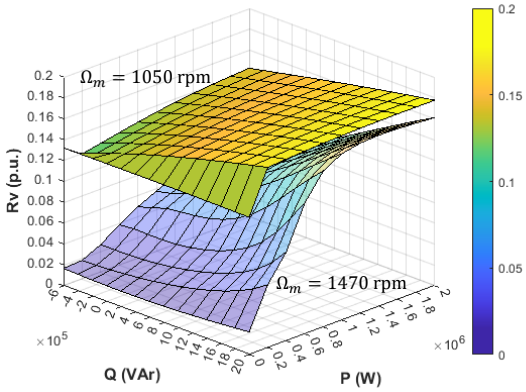

(a)

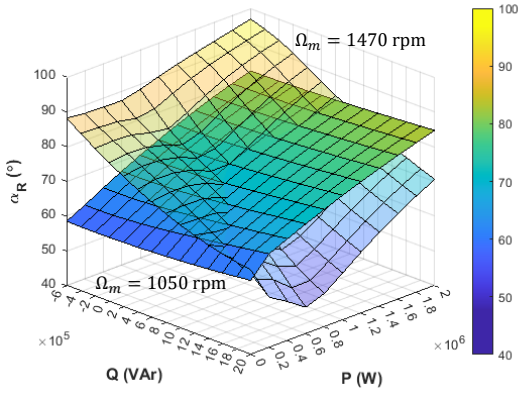

(b)

Fig. 11. Optimal control parameters as a function of active and reactive power for Ω_m=1050 rpm (opaque surface), and Ω_m=1470 rpm (semi-transparent surface): (a) virtual resistor, R_v, and (b) phase rotation, α_R.

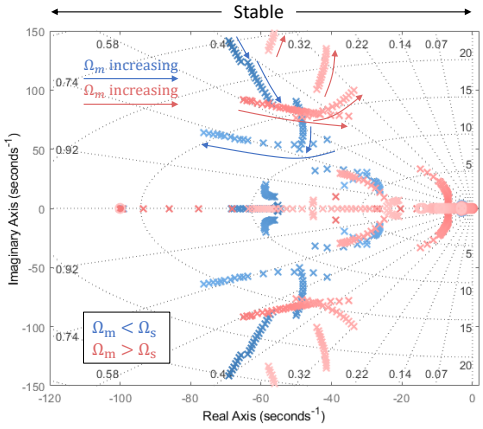

Fig. 12. Evolution of the closed-loop poles with the machine's rotational speed after implementing the proposed control strategy.

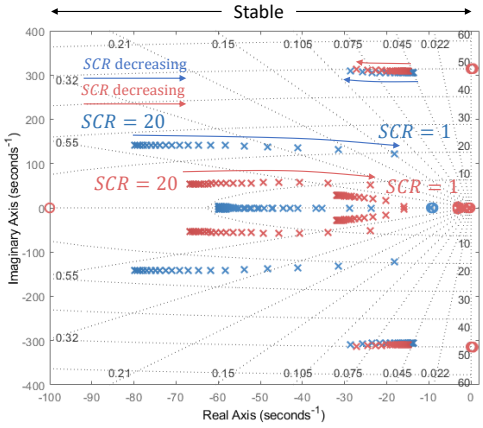

Fig. 13. Evolution of the closed-loop poles with the SCR at Ω_m=1050 rpm (blue), and at Ω_m=1470 rpm (red).

D. Influence of grid impedance on system stability

To ensure system stability, the influence of system parameter variations on system stability must be analyzed. The system parameter that is unknown and may experience the largest variation is the grid inductance. The grid inductance is inversely proportional to the short circuit ratio (SCR) which is an indicator of the grid strength. In Fig. 13 the evolution of the closed-loop poles as a function of the SCR is plotted for Ω_m=1050 rpm (blue), and Ω_m=1470 rpm (red). As can be seen, the system remains stable in both strong and weak grids, even with a SCR equal to 1. Therefore, it is shown that the proposed control strategy is robust to grid strength variations.

E. Single-loop vs multi-loop droop control

Now, the performance of the proposed single-loop droop control strategy is compared with a classical multi-loop control method applied to DFIG wind turbines.

For this purpose, the test system shown in Fig. 14 has been developed in $MATLAB/Simulink$, and the performance of both single-loop and multi-loop droop control strategies has been analyzed through simulation. The system consists of a synchronous generator and a DFIG wind turbine connected through an electrical line feeding a variable resistive load, R_{load}. The SG together with the transformer, modeled by $X_{t,SG}$ equal to 0.1 p.u., and the line reactance, $X_{L,SG}$, models the grid to which the DFIG wind turbine is connected through the step-up transformer, modeled by $X_{t_{DFIG}}$ equal to 0.085 p.u., and the line reactance $X_{L_{DFIG}}$ equal to 0.1 p.u. It should be noted that the line reactance, $X_{L,SG}$ has been considered variable to simulate points near or far from the power grid. The SG is modeled with an alternator, an excitation system and a speed and steam turbine regulation system, whose models and parameters are specified in the Technical standard for monitoring the compliance of power generating modules according to EU Regulation 2016/631. The alternator is a smooth rotor SG. The excitation system is represented by the IEEE model type ST1 (according to IEEE standard 421.5) and the speed and steam turbine regulation system is represented by the IEEE model type 1 (IEEEG1).

In this scenario, the response of the DFIG wind turbine to load variations and unbalances has been analyzed when the proposed single-loop droop control and a multi-loop droop control strategy are implemented. More specifically, the proposed single-loop droop control strategy has been compared with the indirect stator flux orientation (ISFO)-based droop control applied in [10]–[13].

Firstly, the response of the DFIG wind turbine to load variations has been analyzed. A variation in the power demanded by the load has been simulated, and the evolution of the power generated by the DFIG wind turbine has been compared with both control strategies. As shown in Fig. 15, at the beginning of the simulation, a resistive load of 1 p.u. is connected, demanding an active power of about 1 p.u., and both the SG and the DFIG wind turbine generate an active power of about 0.5 pu. At 30 s, a three-phase resistive load of 5 p.u. is connected in parallel increasing the power demand by 20%. As can be observed, the response provided by both single-loop and multi-loop droop control strategies to this load variation is practically identical. This is because both controls implement the same synchronization loop with the same droop coefficient. Additionally, both the SG and the DFIG increase the generated power in the same ratio since they have the same droop. However, the SG exhibits a slower response due to the slow dynamics of the steam turbine.

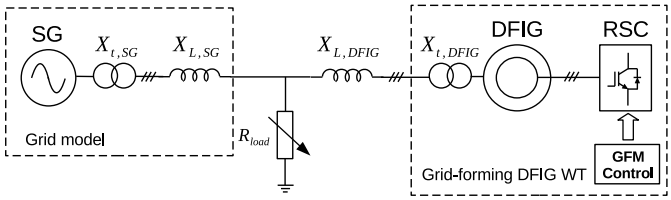

Fig. 14. Developed test system to compare single-loop vs multi-loop droop control performance under load variations and unbalances.

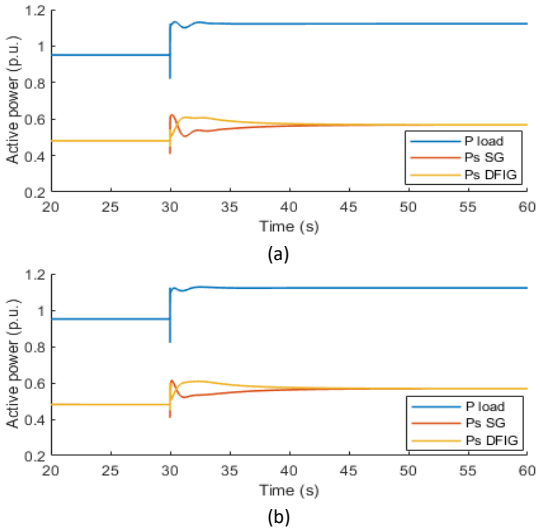

Fig. 15. SG and DFIG power response to a load variation: (a) applying the proposed single-loop droop control, and (b) applying the multi-loop droop control.

TABLE II
INVERSE SEQUENCE DFIG CURRENT AND LOAD VOLTAGE

	$X_{L,SG}$ (p.u.)	I^-_{DFIG} (p.u.)	V^-_{load} (p.u.)
Single-loop control	0.1	0.0465	0.0140
	0.4	0.0539	0.0162
Multi-loop control	0.1	0.0341	0.0173
	0.4	0.0426	0.0208

Secondly, the performance of both control strategies under unbalanced loads has been analyzed. The connection of a resistive load in one of the phases has been simulated and the inverse sequence stator current of the DFIG, I^-_{DFIG}, and the inverse sequence voltage of the load, V^-_{load}, have been obtained. The simulation results are provided in Table II. In these simulations the impact of grid strength on the supply of inverse sequence currents has been observed. In a strong grid, with $X_{L_{SG}}$ equal to 0.1 p.u., most of the inverse sequence current is supplied by the SG since it has a lower inverse sequence impedance. Consequently, the differences between the two control strategies are relatively small. When applying the proposed single-loop droop control strategy the inverse sequence voltage of the load is 0.0140 p.u., while with the multi-loop droop control strategy it is 0.0173 p.u.

However, in a weak grid, with $X_{L_{SG}}$ equal to 0.4 p.u., higher differences can be observed. In weak grids, the generation units closer to the loads are responsible for supplying the inverse sequence current required by unbalanced loads. In this scenario, it can be seen that the single-loop droop control proposed in this paper exhibits a lower inverse sequence impedance, providing a higher inverse sequence current and resulting in a lower distortion in the load voltage. As shown in Table II, with the proposed single-loop droop control strategy the inverse sequence voltage of the load is 0.0162 p.u., while with the multi-loop droop control strategy it is 0.0208 p.u. This may be one of the advantages of the proposed single-loop droop control over the multi-loop droop control.

V. EXPERIMENTAL RESULTS

The proposed single-loop droop control strategy is validated through experimental results in the experimental setup shown in Fig. 16. The setup is formed by a doubly-fed induction generator connected to a permanent magnet servomotor used as driving machine. The rotor windings are directly connected to a three-phase two-level power converter, whereas the stator is connected through a series inductor to the Cinergia GE&EL-30 grid emulator. DFIG and converter control parameters are provided in Table III. The DC bus of the converter is powered by the AMETEK SPS400x75-K12D DC voltage source. The power converter is controlled by means of a dSpace DS1104 and the results captured with the oscilloscope Tektronix MDO3054.

As a previous step to analyze the effectiveness and performance of the proposed control strategy, the stator voltage and current waveforms captured with the oscilloscope have been checked. Fig. 17 shows the stator voltage and current waveforms when a step from 0 W to 500 W is introduced in the active power reference operating at 1050 rpm. In yellow the RS line voltage is represented and in blue the R phase current. As can be seen, both voltage and current have a sinusoidal waveform with low THD.

To prove the effectiveness of the proposed control strategy, the active power evolution is analyzed as the proposed control solutions are disabled. Fig. 18 (a) and Fig. 18 (b) show the active power evolution at 1050 rpm and 1470 rpm, respectively, when the proposed control solutions are activated

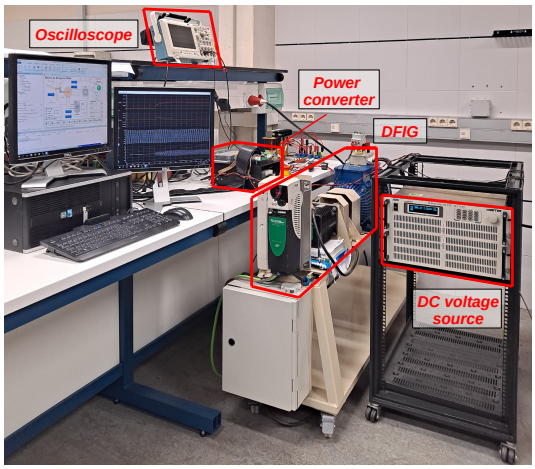

Fig. 16. Experimental setup formed by a three-phase power converter connected to the rotor of a doubly-fed induction generator.

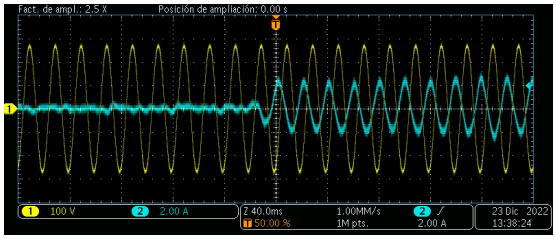

Fig. 17. Stator voltage and current waveforms.

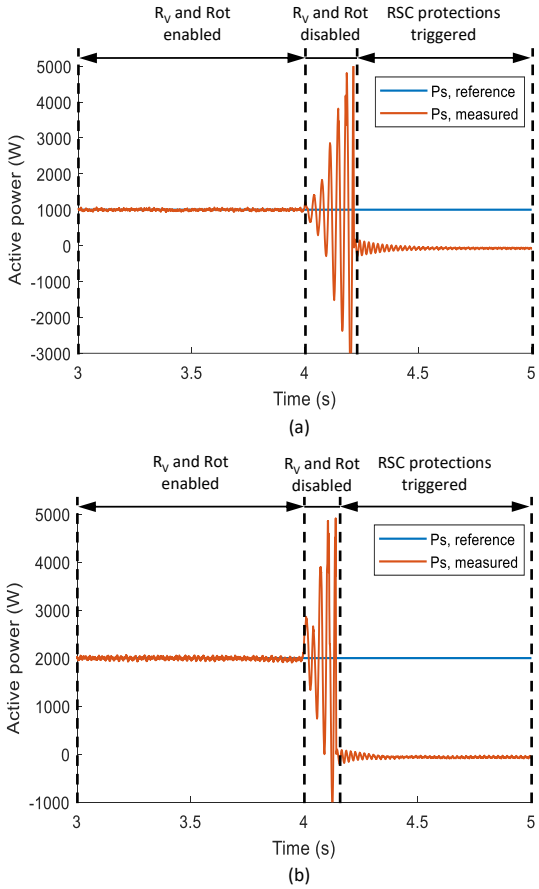

Fig. 18. Active power evolution disabling the proposed control solutions at 4 s: (a) at Ω_m=1050 rpm, and (b) at Ω_m=1470 rpm.

and deactivated. At the beginning of the test, when the virtual resistor and the phase rotation are enabled, it is observed how the active power perfectly tracks its reference, 1000 W at 1050 rpm and 2000 W at 1470 rpm. However, when both the virtual resistor and phase rotation are disabled at 4 s, the system is destabilized and the converter protections are triggered to avoid overcurrents. These results show how the virtual resistor and phase rotation stabilize the system proving the effectiveness of the proposed control strategy.

TABLE III
TEST BENCH PARAMETERS

Parameter	Magnitude
Grid $U_g = 200\ V$, $F_g = 50\ Hz$	
Line inductance	2.2 mH
DFIG (referred to stator) $S_{DFIG} = 5\ kVA$, $U_{DFIG} = 200\ V$	
Rotor resistance	1.1 Ω
Rotor leakage inductance	2.2 mH
Stator resistance	1.3 Ω
Stator leakage inductance	5.7 mH
Mutual inductance	43.7 mH
Pole pairs	2
Power converter control parameters	
Sampling frequency	5 kHz
P-f droop coefficient	0.05 p.u.
PI proportional gain	0.004 V/VAr
PI integral time constant	0.01 s
Time constant of low-pass analog filters	3.10^{-5} s

Now, the performance of the proposed control strategy is validated in terms of active and reactive power reference tracking. For this, the power step response obtained in the test bench is compared to the step response of the simulation model built in $MATLAB/Simulink$. Fig. 19 and Fig. 20 show the active and reactive power evolution at 1050 rpm and 1470 rpm, respectively. In Fig. 19 (a) the active and reactive power is represented when a step from 0 W to 1000 W is introduced in the active power reference at a unit power factor, while in Fig. 19 (b) the active and reactive power is represented when a step from 0 VAr to 1000 VAr is introduced in the reactive power reference keeping the active power reference at 1000 W. In Fig. 20 (a) the active and reactive power is represented when a step from 1000 W to 2000 W is introduced in the active power reference operating at unit power factor, while in Fig. 20 (b) the active and reactive power is represented when a step from 1000 VAr to 2000 VAr is introduced in the reactive power reference, keeping the active power reference at 2000 W. As can be proved, both the active and reactive power track the desired references and exhibit similar dynamics in the experimental setup and in the model built in $Simulink$. The differences observed are due to the harmonics introduced by the test bench machine. As it is a low power machine, 5 kW, the construction techniques used in its manufacture differ from those used in high power machines, so that harmonics are not

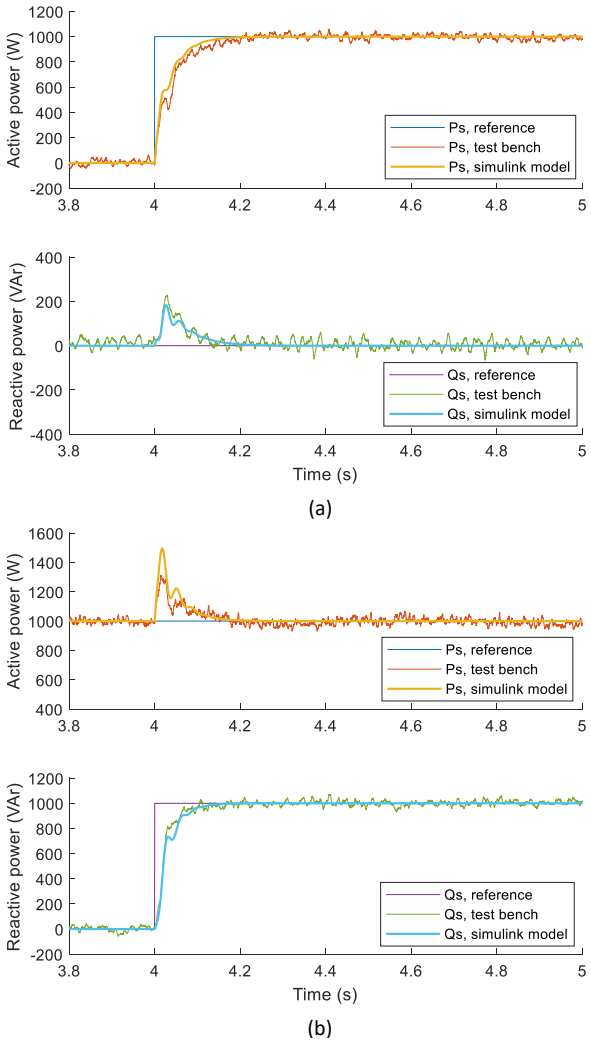

Fig. 19. Experimental and simulation step-response at Ω_m=1050 rpm: (a) active power step response and (b) reactive power step response.

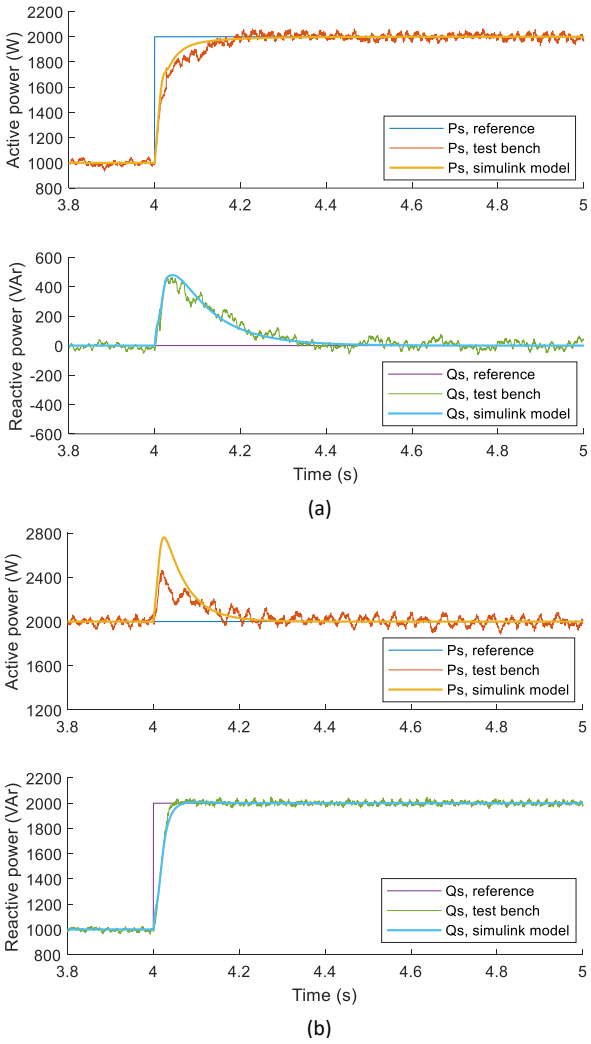

Fig. 20. Experimental and simulation step-response at Ω_m=1470 rpm: (a) active power step response and (b) reactive power step response.

completely eliminated. These effects are not included in the $Simulink$ model.

Finally, the system response to grid frequency variations is analyzed to demonstrate that the proposed droop control strategy provides frequency support. Fig. 21 shows the active power evolution at 1050 rpm and 1470 rpm, when a grid frequency variation is produced. In Fig. 21 (a) the active power is represented when a frequency variation from 50 Hz to 49.6 Hz is produced operating at 1050 rpm, while in Fig. 21 (b) the active power is plotted when a frequency deviation from 50 Hz to 50.4 Hz is produced at 1470 rpm. As can be observed, when the frequency decreases the output power increases, while when the frequency increases the output power decreases. The output power varies according to the defined P-ω droop coefficient, m_p. A droop coefficient m_p equal to 5 % has been defined, and a frequency variation equal to 0.8 % has been produced so the output power should vary by 16 %. As can be seen in Fig. 21, the power varies around 800 W which is equivalent to 16 % of the rated power. Therefore, it is shown that the proposed control provides the desired frequency support to grid frequency variations.

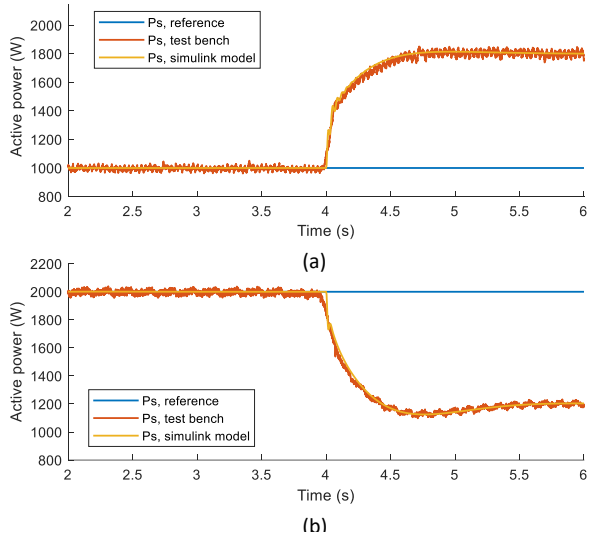

Fig. 21. Experimental and simulation response to grid frequency variations: (a) at Ω_m=1050 rpm, and (b) at Ω_m=1470 rpm.

The experimental results demonstrate that the control solutions proposed in Section IV allow to stabilize the system response at all rotational speeds and at all active and reactive power levels. Furthermore, by optimizing the control parameters, a fast and damped active and reactive power response is achieved. Finally, the system response to grid frequency variations demonstrates the capability of the proposed droop control strategy to provide frequency support.

VI. Conclusion

This paper proposes the application of a single-loop droop control strategy to a grid-connected DFIG wind turbine, unlike the conventional approach where inner control loops are typically used. However, as shown in the paper, the application of the conventional droop control without inner control loops to DFIG-based wind power systems does not ensure a stable response. After modeling the system dynamics and evaluating its stability, two causes of instability are identified; a resonance at the rotor electrical frequency, relevant at high slips, and a phase margin reduction at low slips. To address these instability issues, two control solutions are suggested. The first solution involves emulating a virtual resistor that damps the resonance that causes the instability at high slips. The second solution consists in the introduction of a rotation that increases the phase margin in the most restrictive eigenvalue, solving the second cause of instability. As experimental results show, the combination of both control solutions allows stabilizing the system and achieving a fast and damped dynamic response at all rotational speeds and at all active and reactive power levels. Therefore, the paper demonstrates that it is feasible to apply a single-loop droop control strategy to a DFIG wind turbine.

Acknowledgment

The authors would like to thank Ingeteam Power Technology for its support.

References

[1] I. Oraa, J. Samanes, J. Lopez, and E. Gubia, "Control strategy for a droop-controlled grid-connected dfig wind turbine," in *2022 IEEE 23rd Workshop on Control and Modeling for Power Electronics (COMPEL)*, DOI 10.1109/COMPEL53829.2022.9830010, pp. 1–7, 2022.

[2] E. Commission, J. R. Centre, and T. Telsnig, *Wind Energy Technology Development Report 2020*. Publications Office of the European Union, 2021.

[3] J. O'Brien, "Managing system strenth during the transition to renewables," GHD Advisory, Tech. Rep., 2020.

[4] R. Rosso, X. Wang, M. Liserre, X. Lu, and S. Engelken, "Grid-forming converters: Control approaches, grid-synchronization, and future trends—a review," *IEEE Open Journal of Industry Applications*, vol. 2, DOI 10.1109/OJIA.2021.3074028, pp. 93–109, 2021.

[5] D. B. Rathnayake, M. Akrami, C. Phurailatpam, S. P. Me, S. Hadavi, G. Jayasinghe, S. Zabihi, and B. Bahrani, "Grid forming inverter modeling, control, and applications," *IEEE Access*, vol. 9, DOI 10.1109/ACCESS.2021.3104617, pp. 114 781–114 807, 2021.

[6] H. Zhang, W. Xiang, W. Lin, and J. Wen, "Grid forming converters in renewable energy sources dominated power grid: Control strategy, stability, application, and challenges," *Journal of Modern Power Systems and Clean Energy*, vol. 9, DOI 10.35833/MPCE.2021.000257, no. 6, pp. 1239–1256, 2021.

[7] J. M. Guerrero, J. C. Vasquez, J. Matas, L. G. de Vicuna, and M. Castilla, "Hierarchical control of droop-controlled ac and dc microgrids—a general approach toward standardization," *IEEE Transactions on Industrial Electronics*, vol. 58, DOI 10.1109/TIE.2010.2066534, no. 1, pp. 158–172, 2011.

[8] J. Rocabert, A. Luna, F. Blaabjerg, and P. Rodríguez, "Control of power converters in ac microgrids," *IEEE Transactions on Power Electronics*, vol. 27, DOI 10.1109/TPEL.2012.2199334, no. 11, pp. 4734–4749, 2012.

[9] W. Du, Z. Chen, K. P. Schneider, R. H. Lasseter, S. Pushpak Nandanoori, F. K. Tuffner, and S. Kundu, "A comparative study of two widely used grid-forming droop controls on microgrid small-signal stability," *IEEE Journal of Emerging and Selected Topics in Power Electronics*, vol. 8, DOI 10.1109/JESTPE.2019.2942491, no. 2, pp. 963–975, 2020.

[10] L. Huang, H. Xin, L. Zhang, Z. Wang, K. Wu, and H. Wang, "Synchronization and frequency regulation of dfig-based wind turbine generators with synchronized control," *IEEE Transactions on Energy Conversion*, vol. 32, DOI 10.1109/TEC.2017.2675480, no. 3, pp. 1251–1262, 2017.

[11] R. K. Rastogi and R. Sharma, "Improved synchronization and voltage regulation of dfig based wind energy system (wes)," in *2018 International Conference on Current Trends towards Converging Technologies (ICCTCT)*, DOI 10.1109/ICCTCT.2018.8551121, pp. 1–5, 2018.

[12] Y. Han and J.-I. Ha, "Droop control using impedance of grid-integrated dfig within microgrid," *IEEE Transactions on Energy Conversion*, vol. 34, DOI 10.1109/TEC.2018.2861819, no. 1, pp. 88–97, 2019.

[13] H. Xiao, Z. Zhao, K. Zhou, J. Guo, C. S. Lai, and L. Lei Lai, "Voltage-source control of dfig in standalone wind power-based microgrids," in *2020 IEEE 1st China International Youth Conference on Electrical Engineering (CIYCEE)*, DOI 10.1109/CIYCEE49808.2020.9332674, pp. 1–7, 2020.

[14] Z. Xie, X. Gao, S. Yang, and X. Zhang, "Improved fractional-order damping method for voltage-controlled dfig system under weak grid," *Journal of Modern Power Systems and Clean Energy*, DOI 10.35833/MPCE.2020.000843, pp. 1–10, 2021.

[15] Z. Miao, "Impedance-model-based ssr analysis for type 3 wind generator and series-compensated network," *IEEE Transactions on Energy Conversion*, vol. 27, DOI 10.1109/TEC.2012.2211019, no. 4, pp. 984–991, 2012.

[16] H. Liu, X. Xie, C. Zhang, Y. Li, H. Liu, and Y. Hu, "Quantitative ssr analysis of series-compensated dfig-based wind farms using aggregated rlc circuit model," *IEEE Transactions on Power Systems*, vol. 32, DOI 10.1109/TPWRS.2016.2558840, no. 1, pp. 474–483, 2017.

[17] I. Oraa, J. Samanes, J. Lopez, and E. Gubia, "Modeling of a droop-controlled grid-connected dfig wind turbine," *IEEE Access*, vol. 10, DOI 10.1109/ACCESS.2022.3142734, pp. 6966–6977, 2022.

[18] J. Samanes, A. Urtasun, E. L. Barrios, D. Lumbreras, J. López, E. Gubia, and P. Sanchis, "Control design and stability analysis of power converters: The mimo generalized bode criterion," *IEEE Journal of Emerging and Selected Topics in Power Electronics*, vol. 8, DOI 10.1109/JESTPE.2019.2941829, no. 2, pp. 1880–1893, 2020.

[19] T. Qoria, Q. Cossart, C. Li, X. Guillaud, F. Colas, F. Gruson, and X. Kestelyn, "Deliverable 3.2: Local control and simulation tools for large transmission systems," MIGRATE project, Report, 2018. [Online]. Available: https://www.h2020-migrate.eu/downloads.html

[20] J. Samanes, L. Rosado, E. Gubia, and J. Lopez, "Sub-synchronous resonance damper based on the stator voltage feedback for dfig wind turbines," in *2020 IEEE 21st Workshop on Control and Modeling for Power Electronics (COMPEL)*, DOI 10.1109/COMPEL49091.2020.9265761, pp. 1–8, 2020.

Iker Oraa was born in Pamplona, Spain, in 1996. He received the B.Sc. and the M.Sc. degree in industrial engineering, in 2018 and 2020, respectively, from the Public University of Navarre (UPNA), Pamplona, Spain. In 2020, he joined the Electrical Engineering, Power Electronics and Renewable Energy Research Group (INGEPER), UPNA. His research interests include renewable energies and control of power electronics.

Javier Samanes (S'15 - M'18) was born in Pamplona, Spain, in 1990. He received the M.Sc. degree in electrical engineering from the Public University of Navarre (UPNA), Pamplona, Spain, in 2014 and the M.Sc. degree in renewable energy engineering in 2016 from the same institution. He obtained the Ph.D. degree in electrical engineering from the UPNA in 2018.

In 2014, he joined the Electrical Engineering, Power Electronics and Renewable Energy Research Group (INGEPER) at the UPNA, where he is currently Assistant Professor and member of the Institute of Smart Cities (ISC). In 2018 he was visiting scholar in the Center for Power Electronic Systems (CPES) at Virginia Tech, USA. His research interests include power electronics and renewable energies.

Jesus Lopez (M'05) was born in Pamplona, Spain, in 1975. He received the M.Sc. degree in industrial engineering from the Public University of Navarra, Pamplona, Spain, in 2000. In 2008 he received the Ph.D. degree in industrial engineering from the Public University of Navarra, Spain, in collaboration with the LAPLACE laboratory, Toulouse, France.

In 2001, he joined the Power Electronic Group, Electrical and Electronic Department at the Public University of Navarra, where he is currently an Assistant Professor and is also involved in research projects mainly in co-operation with industry. His research interests are in the field of power electronics, power systems quality and renewable energies, such as wind turbines and photovoltaic plants.

Eugenio Gubia (M'04) received the M.Sc. and Ph.D. degrees in industrial engineering from the Public University of Navarre, Spain, in 1995 and 2003, respectively.

He joined the Electrical and Electronic Department of the Public University of Navarre in 1996, where he is currently an associate professor and member of the Institute of Smart Cities (ISC). In 2002, he joined the Electrical Engineering, Power Electronics, and Renewable Energy Research Group (INGEPER). From June to December 2005, he worked as a guest researcher at the Center for Power Electronics Systems (CPES) in the field of electromagnetic compatibility. His research interests are in the field of power electronics, renewable energy systems, high-frequency phenomena, and electromagnetic compatibility.